J. Space Weather Space Clim. 2025, **15**, 13

https://doi.org/10.1051/swsc/2025009

JSWSC

Available online at:
www.swsc-journal.org

RESEARCH ARTICLE OPEN ACCESS

Robust reanalysis of the electron radiation belt dynamics for physics driven space climatology applications

Nour Dahmen[1,*], Constantinos Papadimitriou[2], Antoine Brunet[1], Angélica Sicard[1], Sigiava Aminalragia-Giamini[2], and Ingmar Sandberg[2]

[1] DPHY, ONERA, Université de Toulouse, 31000 Toulouse, France
[2] SPARC – Space Applications and Research Consultancy, 105 51 Athens, Greece

Received 4 July 2024 / Accepted 10 March 2025

Abstract – Specification models for radiation belts are essential for the design of radiation resistant, long-lasting spacecraft. Using the available in-situ measurements allows these models to virtually describe the average space radiation environment. However, their dependence on observations will make them suffer from data gaps which may lead to poor assessment of degradation risks. To counter this problem, one can have access to continuous descriptions of the radiation belt dynamics on long time periods through climate reanalysis. This operation consists in the assimilation of historical measurements in radiation belt simulations over solar-cycle-long periods, allowing for a physics-based filling of data gaps and the re-calibration of the radiation belt codes on long simulations. The obtained database of continuous historical distributions may serve later in the elaboration of space climatology models and a new generation of physics-based specification models. Yet, the success of climate reanalysis operation is strongly dependent on the numerical stability of the data assimilation procedure that can be deteriorated in the low earth orbit region for instance. Hence, we present in this paper, the climate reanalysis of the trapped electron dynamics using the Salammbô code for the 2014–2022 period, with promising results when compared to standard specification models. We also present the methodology followed to stabilize the assimilation in the low earth orbit.

Keywords: Electron radiation belts / Specification models / Climate reanalysis

1 Introduction

Space radiations represent an inherent challenge to the space industry (Koons et al., 1999). Among all the different sources from which they may originate (Bourdarie & Xapsos, 2008), Earth's electron radiation belts play a significant role in this constant threat as they span over the majority of satellite orbits.

Especially, the exposure of spacecraft to this highly energetic (100 keV to few MeV's) particle population can lead to the build-up of charges on internal surfaces, triggering electrostatic discharges on critical components (internal charging risk) or a cumulative deterioration of materials due to the energy deposit by incident particles (ionising dose) (Gubby & Evans, 2002). Besides, the magnetic trapping of electrons in the radiation belts and their coupling with solar activity, leads to the modulation of their complex dynamic from the scale of geomagnetic perturbations (few days) to the scale of solar cycle variations (Abel et al., 1994; Hudson et al., 2008).

The accurate specification of this environment and its long-term variations, directly impact the design assumptions of space vehicles and their effective operating lifetime. Till today, the design process rely on widely-adopted standard models either describing the electron radiation belt global environment such as AE8 (Vette, 1991), AE9 (Ginet et al., 2014) or local models dedicated to certain orbits or regions in the radiation belts, such as IGE-2006 (Sicard-Piet et al., 2008) for the GEO orbit. Also referred to as empirical models (as their construction rely mainly on observations from different satellite missions), they provide averaged descriptions of the electron flux, that can be modulated by solar cycle (Sicard et al., 2018) along with uncertainty estimations (Ginet et al., 2014). Yet, this close dependency to in-situ data is also responsible for these models limitations. Indeed, their accuracy will always remain sensitive to the challenges related to their underlying data, both in term of availability (gaps in time, space, energy channels) and of representativeness (counts to flux conversion, magnetic coordinates conversion). This aspect leads to the major differences reported in several comparisons with averaged in-flight data even during moderate times (Caron et al., 2022, 2024).

*Corresponding author: nourallah.dahmen@onera.fr

Nevertheless, one can still have access to reliable and continuous historical radiation belt distributions through the combination of radiation belt modelling codes such as Salammbô (Beutier & Boscher, 1995) and data assimilation (Bourdarie & Maget, 2012; Brunet et al., 2023). Much like its early adoption in atmospheric science, this operation called climate reanalysis (Slivinski, 2018), consists in the assimilation of past observations over years of simulated radiation belt dynamics leading to the production of a database of simulated historical distributions. The latter might serve later as a basis to carry out climatology studies or to manufacture specification models, using appropriate statistical studies. Hence, climate reanalysis offers to tackle the above-mentioned sparsity limitation of ingested data with a physics-driven data reconstruction. Also, the continuity of the ingested data will help improve the characterizations of extreme events by the newly manufactured specification models instead of rough worst case scenarios (Ripoll et al., 2020) which will be useful in preparation for stronger solar cycles (Lugaz et al., 2023).

The application of climate reanalysis in the context of space climatology is not recent. The methodology was followed in the of ONERA's Outer Zone Electrons (OZONE) model, a specification model for the outer belt (Bourdarie et al., 2009). For that, 17 years of the trapped electrons dynamics were simulated with Salammbô and reanalysed with the direct insertion assimilation method. Then, a statistical study was conducted on the obtained flux maps which provided yearly averaged states of the electron outer belt depending on the solar cycle year. Lately, the methodology was redeployed on a new time period spreading over a different solar cycle, with the provision of new sources of data as well as the adoption of a new robust, accurate and fast numerical solver in addition to the Ensemble Kalman Filter (EnKF) (Dahmen et al., 2024). These improvements along with the now relatively small computational cost of Salammbô data assimilation simulations, justify the construction of new reanalysis databases for trapped electrons and protons for future climatology applications. In this paper, we will focus on electrons and we leave the proton case for a future study. Besides, it focuses on evaluating the ability of the reanalysis operation to reconstruct historical distributions over a selected period, leaving the curation of the appropriate period to be simulated for future works.

Until recently, few challenges remained to be addressed to exploit the potential of climate reanalysis over the complete domain of the electron radiation belts. Specifically, the accuracy of the reanalysis databases can be severely impacted in regions where data assimilation can be highly constrained numerically. These constraints can induce nefarious numerical artefacts, that usually appear for the electrons in the inner zone or at low altitude. This is where distributions encounter strong gradients, especially at the end of the magnetic field lines where they meet Earth' upper atmosphere (Bourdarie et al., 2009; Brunet et al., 2023). In Salammbô, the frontier of the drift loss cone is represented by a boundary on the solving domain that excludes particles with drift shells that have a mirror point altitude below 100 km for at least one longitude.

Instead of cumbersome mesh refinement in those locations, the paper suggests, among other things, a procedure to tackle this issue by ingesting data from an empirical model, taken as a low altitude boundary condition. By doing so, data assimilation becomes robust in the inner zone and simulations are now able to provide relevant and accurate descriptions in locations where they were previously unreliable.

Table 1. Specifications of the Salammbô-Electron mesh.

Dimension	α_{eq}	Ec	L^*
Grid limits	2°–90°	10 keV–5 MeV (at $L^* = 8$)	1–8
Grid size	34	25	34

This paper is organised as follows. First, we recall the main aspects of the Salammbô code and its associated data assimilation algorithm. Then, we will present the methodology followed to manufacture the new low Earth orbit model. Later, we present an investigation that supports our claim in the role of the model in the stabilisation of assimilation. Finally, the latter will be put in use to establish a reanalysis database describing from 2014 to 2022 period. Then, we evaluate the database's relevance through comparisons with the standard models AE8, AE9 in addition to observations, showing how the climate reanalysis approach can serve as a foundation for future climatology models.

2 Climate reanalysis in the context of the Salammbô code

2.1 The Salammbô Electron radiation belt model

The Salammbô Electron radiation belt model or Salammbô-Electron is part of ONERA's family of physical codes dedicated to radiation belt modelling around Earth (also existing in a proton version (Beutier et al., 1995) and other magnetized planets in the solar system (Jupiter and Saturn) (Sicard & Bourdarie, 2004; Lorenzato et al., 2012; Nénon et al., 2017).

Salammbô-Electron (or Salammbô for simplicity) solves the 3D Fokker-Planck equation to access f [MeV^{-3}s^{-3}] the statistical distribution of magnetically trapped electrons or the phase space density (PSD) function, as expressed in the (Ec, α_{eq}, L^*) phase space, where Ec [MeV] is the electron's kinetic energy, α_{eq} is the particle's equatorial pitch angle with Earth's magnetic field and L^*, the Roederer parameter (Roederer, 1970). The equation, detailed in Brunet et al. (2023), is solved numerically using a finite volume Euler Implicit solver (Dahmen et al., 2020) over a non-uniform mesh describing the 3D (Ec, α_{eq}, L^*) domain as described in Table 1 and Figure 1.

Salammbô includes within its physical description, the main physical processes responsible for the electron radiation belt dynamics :

- Radial diffusion, the main driving process responsible for the injection of particles, using the *Kp*-driven analytical formula from Boscher et al. (2018). The Salammbô grid is constructed to allow for the conservation of the first and the second invariant when radial diffusion is performed.
- Resonant interactions with Very Low Frequency (VLF) waves, responsible for local energizations and precipitations in the atmosphere. Wave-particle interactions induce

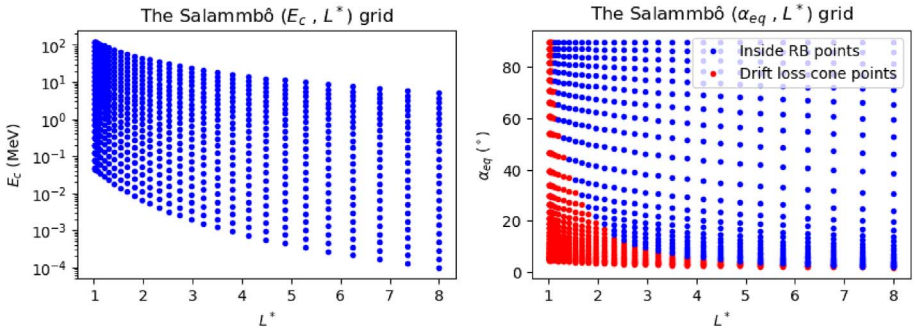

Figure 1. Locations of the Salammbô grid points in (E_c, L^*) and (α_{eq}, L^*).

pitch angle, energy and cross diffusion rates pre-computed for Salammbô by the WAPI code (Sicard-Piet et al., 2014; Dahmen et al., 2022). Thanks to its new finite volume based solver, Salammbô is now able to take into account cross diffusion terms with upstream stability arguments at the additional cost of a non-linear resolution. Regarding the current study, these terms were omitted for computational efficiency (Dahmen et al., 2020). WAPI considers multiple VLF wave emission types sorted depending on their location in the plasmasphere (using the Kp-driven Carpenter & Anderson, 1992 plasmapause model) and their frequency range: plasmaspheric hiss, transmitters and lightning whistlers and plasmatrough upper and lower band chorus. Wave distributions are derived from THEMIS, CRRES, TC1 and DE1 measurements (Meredith et al., 2012; Horne et al., 2013c) with a binning of their intensity based on Kp .

- Interactions with the upper atmosphere's neutrals, free and bound electrons. The induced energy friction and atmospheric diffusion are pre-computed based partly on the MSIS86 density model of the upper atmosphere (Hedin, 1987) driven by the F10.7 and Ap indexes.
- Electron seed population at the external boundary of the radiation belt ready to be injected in its inner layers. The latter is modelled in the code with a boundary condition at $L^* = 8$ based on *THEMIS* data (Maget et al., 2015) and driven by Kp.
- Dropouts by magnetopause shadowing (Li et al., 1997), based on the magnetopause distance computed from the *T89* magnetic field model (Tsyganenko, 1989) driven by Kp as explained in Herrera et al. (2016).

2.2 Previous experiences of climate reanalysis

Following its establishment, Salammbô was coupled with data assimilation algorithms that combine observations with the model's guess to provide best estimates of the radiation belt dynamics (Bourdarie et al., 2005; Maget et al., 2007; Bourdarie & Maget, 2012; Brunet et al., 2023). This approach has now been proven to improve the depiction by physical codes of the outer belt dynamics, during very fast dynamics, despite the many uncertainties preventing the accurate depiction of their driving processes (Tu et al., 2014; Ripoll et al., 2020).

Of all the available assimilation methods, sequential ones were favoured for our application which includes the Kalman Filter (KF) method (Kalman, 1960) and its ensemble adaptation, EnKF method (Evensen, 2003). The latter avoids the huge computational cost of the KF by sampling observation and model's uncertainties using an ensemble of simulation runs. Currently, Salammbô is associated to a data assimilation algorithm implementing the EnKF within the Salammbô-EnKF code (Brunet et al., 2023) and uses tools from the numerical library Parallel Data Assimilation Framework (PDAF) (Nerger et al., 2005). The detailed theoretical development and the equations of the Ensemble Kalman filter are found in Bourdarie & Maget (2012).

Data assimilation application in the radiation belt context is mainly known for space weather prototype applications. This is favored by the growing needs for nowcasting and forecasting the short-term variations of the space radiation environment (Horne et al., 2013a; Brunet et al., 2023). This culminated lately with multiple projects of Sun-to-Earth chains of codes to drive radiation belts dynamics for prototypes of safety warning systems, with a simulated target lead time of few days (Horne et al., 2013b; Dahmen et al., 2023).

Nonetheless, data assimilation can also be considered for space climate applications and specification models through long term data assimilation simulations, or climate reanalysis. Few studies were conducted on electron radiation belt long term dynamics without data assimilation (Glauert et al., 2018). Data assimilation simulations on the other hand were limited to short and medium term time periods up to few years (Subbotin et al., 2011; Cervantes et al., 2020), without a goal to exploit the obtained results for climatology applications. Yet, one can find the application of climate reanalysis to specification model in the example of the OZONE local model, dedicated to the outer electron belt with a solar cycle dependency (Bourdarie et al., 2009). OZONE's foundation relies on the reanalysis of a Salammbô long-term simulation depicting the 1990–2006 period for which assimilated data sources were taken from GEO and GPS orbit satellites along with the CRRES mission.

Lately, it was shown that the OZONE model in particular and the climate reanalysis with Salammbô in general can both benefit from the upgrade of the code's numerical solver along with the ingestion of new sources of data (Dahmen et al., 2024). However, ONERA's climate reanalysis experiences remained limited to the outer belt region. In fact, the extension of the operation to the inner region exposes Salammbô-EnKF and other radiation belt data-assimilation modelling codes to numerical artefacts in a region where the gradients of the phase space density are very strong (Bourdarie et al., 2009;

Dahmen et al., 2023). These gradients are due to the presence of the drift loss cone (near the upper atmosphere limit) implemented in Salammbô as a homogenous boundary condition with a null PSD. One may advocate, as a solution, for the refinement of the α_{eq} grid near the drift loss cone. Yet, this operation will introduce an additional computational cost to the simulation without ensuring additional stability for data assimilation in this region (Dahmen et al., 2023).

3 Electron low earth orbit model

3.1 Data

Data from the Standard Radiation Environment Monitor (SREM) on board the PROBA-1 satellite have been used to build the low altitude model that will play the role of a low altitude boundary conditions during the simulations. The PRoject for On Board Autonomy (PROBA) satellite is a microsatellite of the European Space Agency, funded within the frame of ESA's General Support Technology Program and is part of an overall effort to promote technological missions using small spacecrafts. PROBA1 was launched from Antrix (India) on October 22, 2001 in a Low Earth Orbit (LEO), Sun-synchronous elliptical polar orbit, (with perigee 560, and apogee 672). The mission is dedicated to in-orbit technology demonstration, Earth environment monitoring and preparatory earth observation (Mohammadzadeh et al., 2003).

The SREM instrument, was developed in partnership between ESA, the Paul Scherrer Institute (PSI) for Astrophysics and Contraves Space A.G. It was designed to measure electrons with energies above 500 keV and protons with energies above 10 MeV with fair spectral and angular resolution. The SREM unit consists of three silicon solid-state detectors in two-detectors-head configuration (Evans et al., 2008). Electron data are provided by PSI in the form of mnidirectional, differential fluxes at 10 energy channels, from 650 keV up to almost 2 MeV and are accompanied by quality flags that account for both instrument errors as well as possible contamination by protons.

3.2 Methodology

The main idea of the modelling methodology is, in general lines, the same that has been applied in many historical models in the past and it is to map the measurements in a predefined grid of generalised coordinates. For the purposes of this model, a 3D grid similar to the one employed by Salammbô was used, namely of Energy, equatorial pitch angle α_{eq} and L^*. At the first stage, the energies are those of the SREM instrument, while for both the α_{eq} and L^*, 25 equally-spaced bins were used to cover all angles from 0 to 90 degrees and all L^* from 1 to 8. At this step, all data records between 10/2001 and 04/2023 (the date on which the model was initially designed) are read (keeping only those flagged as of adequate quality) and placed in their corresponding bin. Measurements that were taken within the same day are typically very highly correlated, so all these, in each bin, are averaged thus creating a new grid of daily averaged values of electron fluxes. From these, again independently for each bin, the mean, median and the 25 and 75 percentile values are calculated.

To perform the re-analysis, it was necessary to have boundary conditions at different geomagnetic activity levels.

Table 2. Values of AE-9 fitted parameters.

L^*	B_{AE9}	C_{AE9}
1.75	2.46762329	0.76727529
2.25	2.69113404	0.50572056
2.75	1.66023379	0.75345309
3.25	1.17858189	0.85657367
3.75	1.03541084	0.84057659
4.25	1.06744086	0.81809226
4.75	1.27558428	0.77183547
5.25	1.52898218	0.71591336
5.75	1.64824655	0.76158918
6.25	1.53993163	0.93368255

To implement this, an additional filter was imposed at the data retrieval stage, which selected only measurements that were performed during times for which the Kp index was within certain limits. This allowed the production of four different versions of the model, for quiet (Kp < 2), low (2 ≤ Kp < 4), medium (4 ≤Kp < 6) and high (Kp > 6) geomagnetic disturbance conditions. Kp data were retrieved from the GSFC/SPDF OMNIWeb interface at https://omniweb.gsfc.nasa.gov.

Unfortunately, due to the significantly fewer data that were available for highly disturbed conditions, there were a few cases where bins that were covered by the quiet versions of the model were left empty for some of the disturbed ones. Thankfully, even in these instances only one or two bins were problematic and they were easily filled using a one-dimensional, piece-wise linear interpolation scheme, in which the value of a bin at a certain energy and L^* was estimated by the values of its neighbouring bins at slightly higher and lower α_{eq}. The interpolation was applied at the logarithm of the mean or median flux of the bin and was only used to cover the small, single-bin gaps that appeared. If more than two consecutive bins were empty, a more elaborate method would be required, but thankfully this was not the case for this study.

For the construction of the final model, it is necessary to cover the full energy range of the Salammbô grid, from 10 keV to 5 MeV which demands the application of an extrapolation scheme. In order to avoid extrapolating purely from the data, which can produce very large errors at the tail ends of the extrapolation regime, another method was employed, which relies on the use of another model. The method is as follows. By running the AE9 model, at the orbit of the PROBA-1 satellite, a series of spectra are produced for a wide energy range, from a few keV up to 8 MeV. These spectra are grouped in bins of similar L^* values, for all available values of α_{eq}, and fitted with a law of the form:

$$F(E, L^*) = 10^{A(L^*)} E^{-B(L^*)} e^{-C(L^*)E},$$

where E is the energy in MeV and the three parameters A, B and C are derived from fitting this function on the data, with different fits performed for different L^* values, thus allowing the three parameters to be L^* dependent. The values of these three parameters are then saved in tabular form for different L^*. As is evident, B and C are "shape" parameters that govern the way in which the spectrum decreases for higher energies, while the first parameter A, operates simply as an offset on the log space that determines how high or low the spectrum is positioned. By having these tables, a new fit can then be performed on the values of the fluxes of the model, separately for

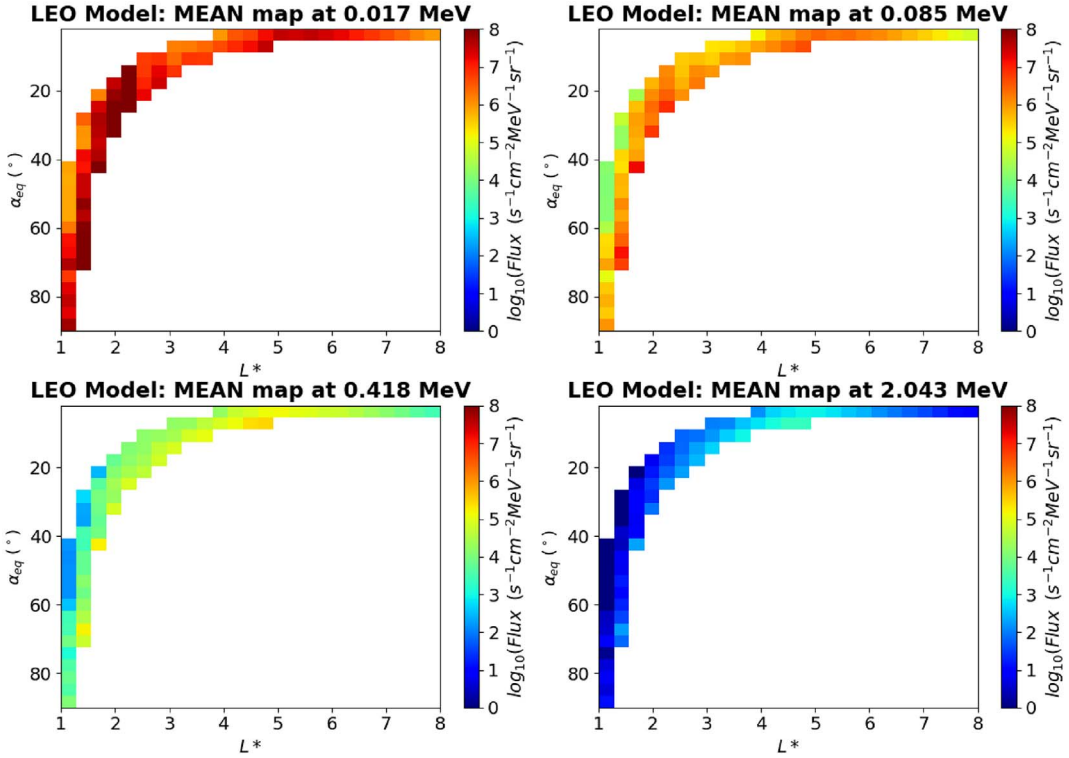

Figure 2. Mean omnidirectional, differential electron fluxes provided by the low altitude model at four indicative energies and at the original α_{eq} vs L^* grid that was used to construct the model.

each grid point in L^* and α_{eq}, but taking into account all energies. In this fit the shape parameters B and C are kept the same as the ones that were derived from the AE-9 fits so they will be named B_{AE9} and C_{AE9} for clarity, and are dependent on L^* alone, and only A is left as a free parameter to be decided by the new fit. Having then the new A and the old B_{AE9} and C_{AE9}, the formula can be used to extrapolate the fluxes to energies both below and above the ones of the dataset, taking the form:

$$F\left(E, L^*, \alpha_{eq}\right) = 10^{A\left(L^*, \alpha_{eq}\right)} E^{-B_{AE9}(L^*)} e^{-C_{AE9}(L^*)E}.$$

The values of the B_{AE9} and C_{AE9} parameters are provided in Table 2.

Performing this on all four versions of the model allows the extension of the energies to the full energy range and energy bin values that are used by the Salammbô grid. This can then be used for the low altitude boundary conditions of the simulations. A snapshot of the model for quiet conditions and at four indicative energies is presented in Figure 2.

4 Reanalysis of the electron radiation belt dynamic over the 2014–2022 period

4.1 Simulation parameters

We simulate the dynamics of the electron radiation belts between 01/01/2014 and 01/01/2023. This period spreads over the ending sequence of the solar cycle 24 with 2014 as a maximum year and the starting sequence of the solar cycle 25 with 2019 as minimum year.

This specific simulation period was chosen as it coincides with a major part of the RBSP mission duration. This period provides to our climate reanalysis operation, tailored and high-fidelity radiation belt observations (Spence et al., 2013). However, the selected period is part of the solar cycle 24 known for its low activity compared to recent solar cycles (Nandy, 2021). In particular, it was marked by weaker solar wind pressure and speed conditions and less geoeffective coronal mass ejections (CMEs) (Nieckarz & Michalek, 2020). This weaker solar activity has been linked to an overall reduction in the intensity of the electron radiation belts. This decrease in activity, well reported by RBSP, GOES and SAMPEX missions, is further evidenced by less frequent but more prolonged flux enhancements, by slower recovery times for the belts following geomagnetic storms more induced by corotating interaction regions (CIRs) and a decrease in multi-MeV electron flux in the slot region and below (Anderson et al., 2015; Rodger et al., 2016; Li et al., 2017; Li & Hudson, 2019). In case of more intense solar wind conditions associated to stronger solar cycles (like the conditions observed during cycle 23 or 22), the behaviour of radiation belts is expected to change significantly, resulting for example in higher relativistic electron fluxes in the outer radiation belt due to more frequent and intense particle injections (as observed by the CRRES mission and earlier GOES satellites). This aspect obviously poses a constraint on the climatology interpretation of the reanalysis database presented in this paper and its representativeness to stronger solar cycles. For instance, the database will be biased by prolonged

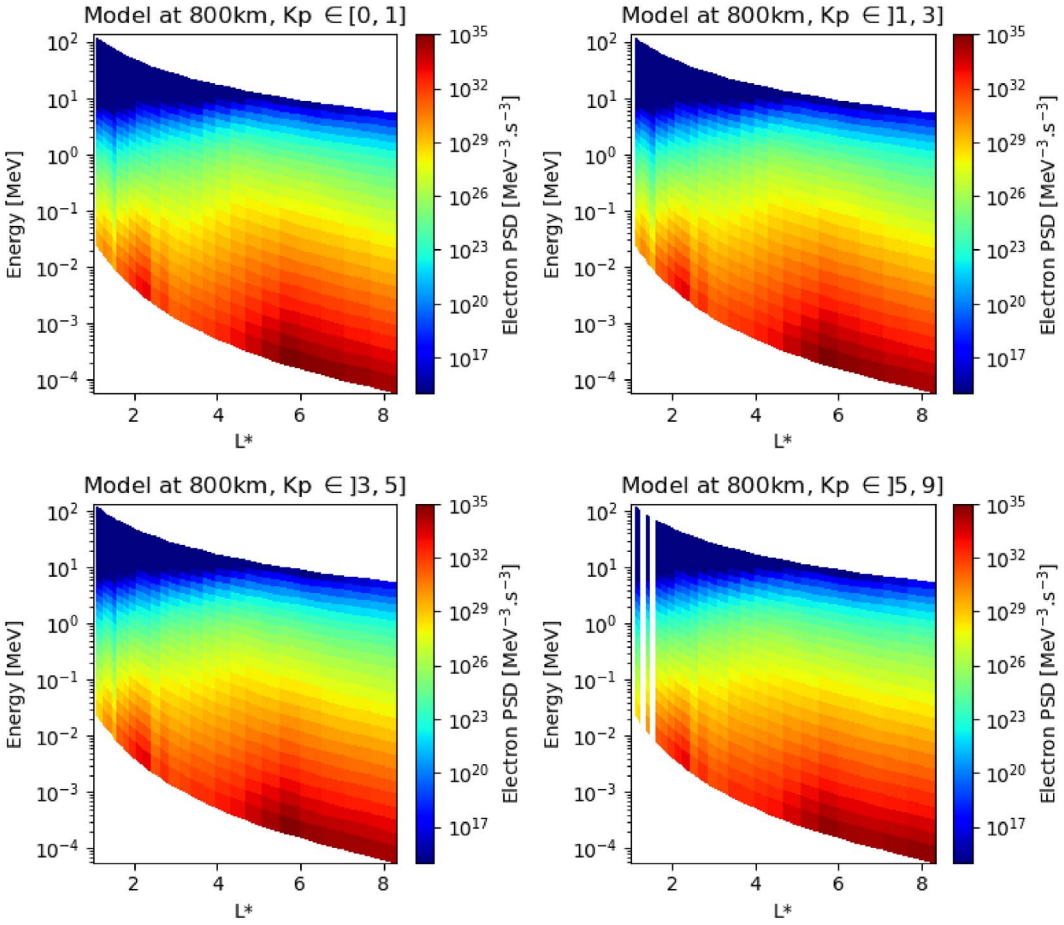

Figure 3. Electron PSD values provided by the low altitude model to Salammbô-EnKF as boundary values at 800 for all the Kp bins.

quiet periods interspersed with moderate storms. Hence, our interpretation of the database's result in the following parts of the article are solely oriented to proof the database's ability to reconstruct historical distributions during the considered time slot. A longer simulation period will be required to fully explore its potential for space climate applications.

The simulation starts from an initial state obtained with an ensemble simulation (no assimilation) of the six months preceding the start of the climate reanalysis period (between 01/07/2013 and 01/01/2014). This operation leaves enough time to spread out the ensemble members. It also allows for a progressive filling of the outer belt from the outer boundary condition.

The unconditional stability of the Salammbô numerical solver allows for a free choice of the integration time step. It was fixed to 100 to ensure time convergence. The EnKF sampling ensemble size was fixed to 100 members, to ensure a stable data assimilation (as recommanded in Bourdarie & Maget, 2012). The construction of the electron re-analysis database required around 5000 h of CPU time, which took 100 wall-clock hours using HPC resources. This computational cost is relatively low given the extended simulated period and the considerable numerical operations performed between the assimilation algorithm and the Salammbô code. This resource-optimized efficiency allowed by the new Salammbô solver, further advocates for the reanalysis approach in the climatology context. Results are saved every hour for the median and every 12 for the ensemble members.

Instead of the usual homogenous boundary condition at the drift loss cone (imposing a null PSD to the grid points located in the drift loss cone), Salammbô ingests for this study, dynamic data from the Electron Low Earth Orbit model (see Sect. 3) as a low-altitude boundary condition. Precisely, the model is applied to Salammbô grid points corresponding to drift-shells with a minimum altitude less than 1500, assuming an eccentric tilted dipole model for Earth's magnetic field, based on the first International Geomagnetic Reference Field (IGRF) moments. The low altitude model and the Salammbô grid share the same energy bins but slightly differ in terms of L^* and y bins. So, the model's PSD values for a given energy are interpolated from its grid to Salammbô grid points where they should be applied using a bilinear interpolation. Those points are represented in Figure 4 (along with the grid points located in the drift loss cone) as we show in Figure 3 the variation of the applied PSD values for different Kp bins.

Table 3 reports the five data sources used by the data assimilation algorithm to construct the electron reanalysis database and the motivation behind their choice. For this application, the ingested data came in the form of Omnidirectional Differential Electron fluxes (FEDO) [s^{-1} cm^{-2} MeV^{-1}] and Unidirectional Differential Electron fluxes (FEDU) [s^{-1} cm^{-2} MeV^{-1} sr^{-1}] as

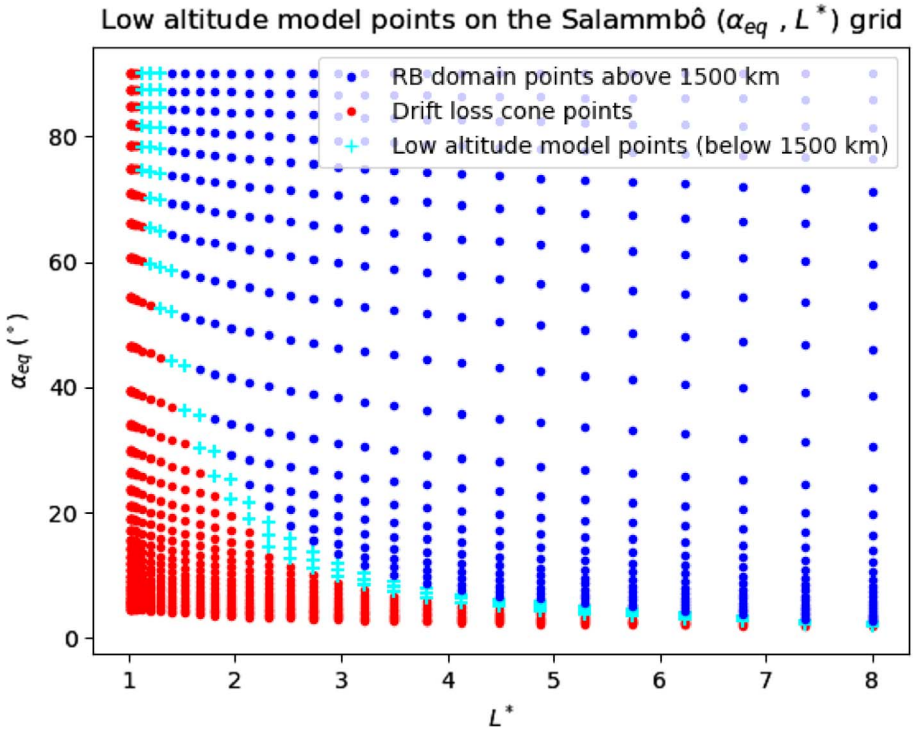

Figure 4. Location of the Salammbô grid points where the low altitude model is applied in comparison to the drift loss cone grid points.

Table 3. Assimilated data used in the construction of the electron re-analysis database.

No	Satellite	Instrument	Flux type	Energy range (MeV)	Assimilation frequency (min)	Assimilation period	Motivation/Comments
1	RBSP A	ECT (Spence et al., 2013)	FEDO	0:05–7	10	2014/01 – 2019/01	Elliptical orbit crossing different L^* values. Orbital plane close to the magnetic equator.
2	RBSP B	ECT	FEDO	0:05–7	10	2014/01 – 2019/01	Same as RBSP A
3	Arase	HEPL XEP (Miyoshi et al., 2018; (Yokota et al., 2019)	FEDO	0:06–3	10	2018/01 – 2021/09	Same as the RBSP satellites. Altitude filter is applied to avoid the Salammbô mesh boundaries
4	GOES15	MAGED (Hanser, 2011)	FEDU	0:2–0:5	10	2014/01 – 2020/01	Smoothing effects from GEO measurements at quasi constant L^*.
5	GPS 72	CXD2F (Morley et al., 2017)	FEDO	0:3–5	10	2018/01 – 2022/31	Orbit crossing the outer belt region.

Salammbô-EnKF is also able to assimilate fluxes in any form (integral or differential in energy, omnidirectional or unidirectional) (Brunet et al., 2023).

4.2 Validation of the low altitude model role in the stabilisation of data assimilation in the inner zone

Before moving to the study of the reanalysis results, we have to demonstrate the utility of new low altitude model. We conducted three different Salammbô-EnKF simulations considering the previously presented simulation parameters but limited to the March–May 2015 period:

- Simulation 1: A data assimilation simulation using the low altitude model.
- Simulation 2: A data assimilation simulation without the low altitude model. This simulation will serve as a reference case prior to the association of the low altitude model to Salammbô-EnKF.
- Simulation 3: A data assimilation simulation without the low altitude model but with the assimilation of observations from the LEO satellite PROBA-V/EPT taken in the form of FEDU fluxes (Pierrard et al., 2019). This simulation will offer an alternative to the low altitude model through the assimilation.

The simulation period was chosen as it contains the 2015 CME-driven *St. Patrick's Day* storm (Li et al., 2016; Baker et al., 2016; Goldstein et al., 2017). During this geomagnetic event, an intense disruption of the electron belt is observed around

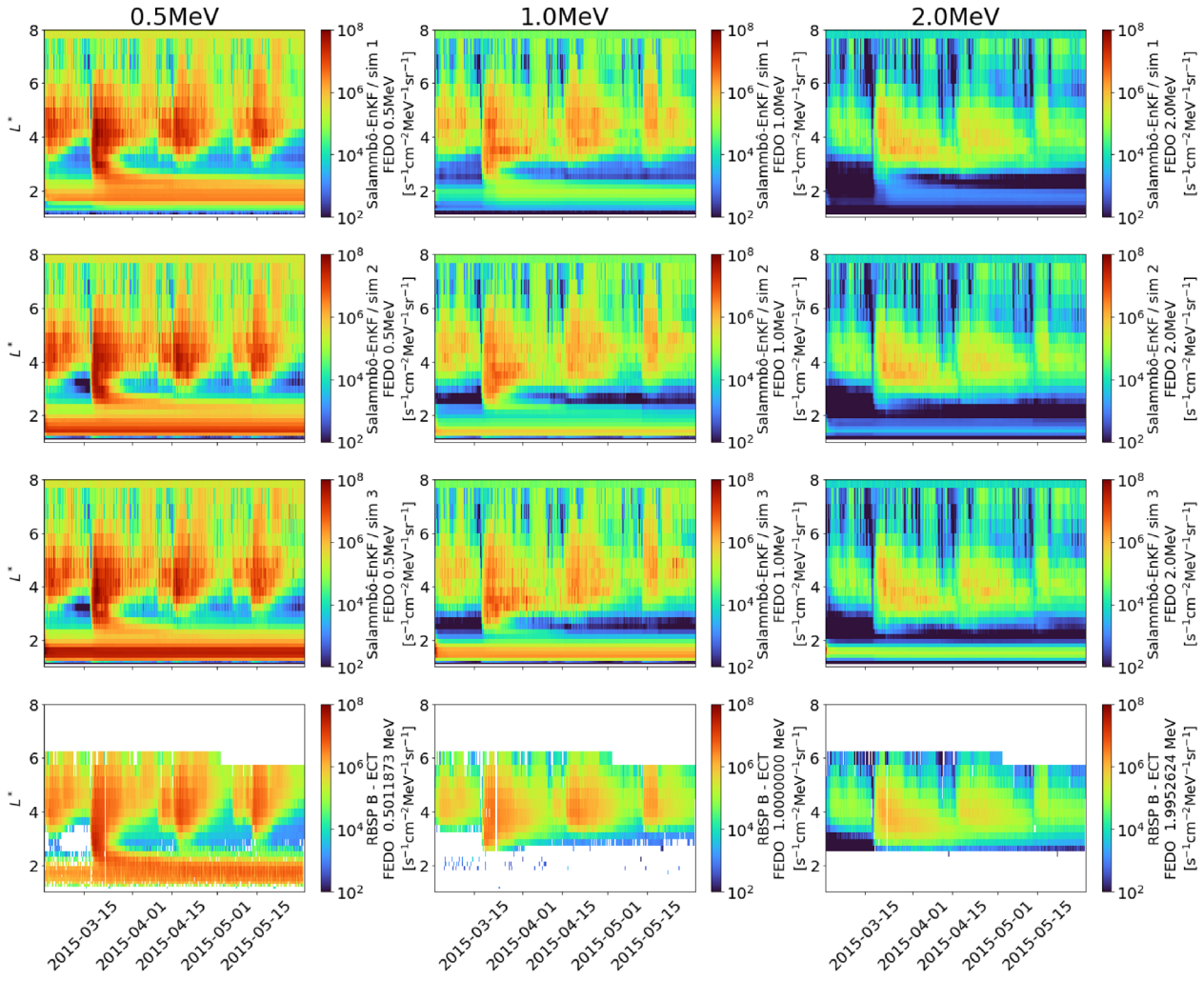

Figure 5. Testing the role of the low altitude model in the stabilization of data assimilation : omnidirectional differential flux estimations of the 0.5 MeV, 1 MeV and 2 MeV electrons (columns) in simulations 1, 2 and 3 (rows) during March, April and May 2015 period, with RBSP-B/ECT measurements.

the middle of March with intense injections down to low L^*. This intensification is a great study case to test the stability of the assimilation. The remaining months of April and May leave enough time ahead of the active period of March to study the propagation or persistence of any numerical artefact that was previously formed. For this test, all three simulations were initialised with only one month-long ensemble simulation (over February 2015) to have enough dispersion between ensemble member while limiting the computational cost. Simulation results are presented in Figure 5 FEDO fluxes at the equator for 0.5 MeV, 1 MeV, 2 MeV along with the observations of these fluxes as seen by the ECT suite onboard of the RBSP-B probe.

First, we can attest that all three simulations report the same behaviour in the outer belt region located at $L^* > 3.5$. Few differences by a factor of 2 may occur within the flux magnitudes at the heart of the outer belt ($L^* \approx 4$) with no incidence on the overall dynamic. This is expected as the outer belt is very dynamic and is driven in the Salammbô code by the external boundary condition and the balance between wave-particle interaction and radial diffusion, with little to no impact from the gradient near the loss cone.

We start to see small differences when we go below the outer belt and enter the slot region. Simulation 1 reports fluxes one order of magnitude higher than in simulation 2 and 3 before March 17th for 500 keV and all the time for 1 MeV. This difference is attributed to the low altitude model and the way it is implemented in the code, by enforcing its data near the drift loss cone where particles are lost through precipitation. In fact, the slot is precisely the place where heavy losses occur due to pitch angle scattering and form a region with a local minimum of flux magnitude (Lyons et al., 1972; Abel & Thorne, 1998). As the low altitude model impacts the emptying rate in the drift loss cone, it will by extension impact the magnitude of the flux minimum. To ensure an accurate description in the slot region, one can thus advocate for the improvement of the low altitude model with the ingestion of additional relevant data from satellites crossing the slot region.

The major differences are seen in the inner zone at all energies. At 500 keV, simulation 1 is closer to RBSP-B

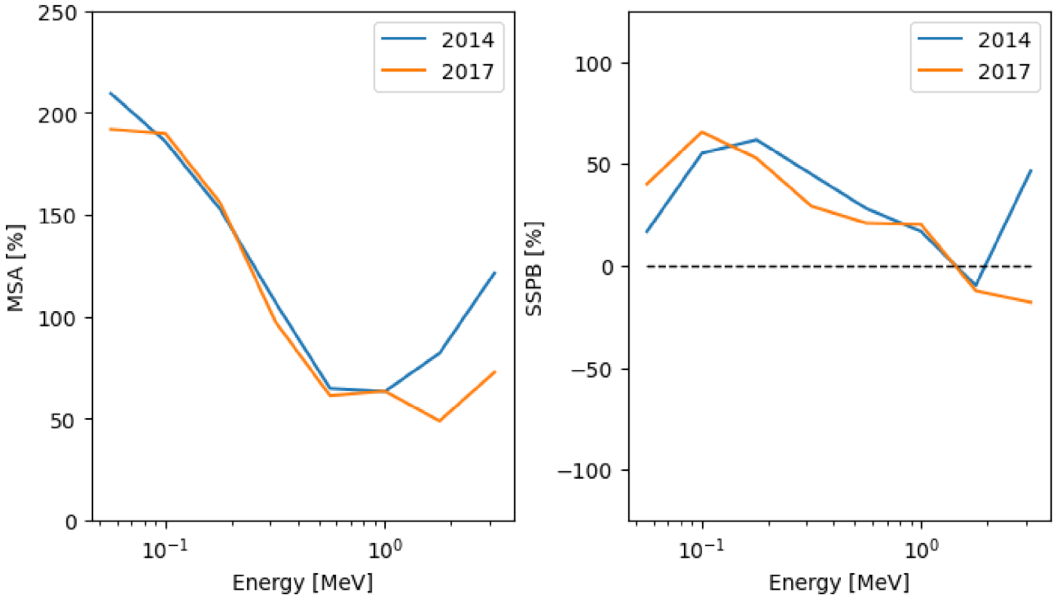

Figure 6. Energy evolution of the Median Symmetric Accuracy (left panel) and Symmetric Signed Percentage Bias (right panel) of the reanalysis database annual averages on RBSP-B/ECT.

observations with a quasi symmetric spread around the peak located around $L^* = 2$. On the other hand, simulations 2 and 3 report an asymmetric inner belt with sharp peaks, significantly below $L^* = 2$, and almost two orders of magnitude higher than in the measurements. Besides, during the main phase of the storm occurring on 17 March, the junction between the inner and outer belt due to strong injections is handled better in simulation 1, while simulations 2 and 3 report a gap above $L^* = 2$ that propagates over time. At higher energies, simulations 2 and 3 report the existence of a strong and consistent inner belt even at 2 MeV and before the injection event of 17 March, unlike what happens in reality (Boscher et al., 2018). On the contrary, 1 and 2 MeV fluxes estimated by simulation 1 in the inner region are much less intense and are strongly linked to the injection event. They also seem to slowly fade away the more we move forward in time which goes in the direction of (Boscher et al., 2018). This odd and non-physical behaviour of the high energy flux seen by simulation 2 and 3 is an example of numerical artefacts that can be encountered in data assimilation simulations. On longer simulations, the latter can be enhanced and even contaminate flux estimations in regions where assimilation is supposed to be more robust.

With this investigation, the low altitude model's contribution to stabilise assimilation in the inner zone is clear. This opens the way for a more reliable long term climate reanalysis.

4.3 Results

The success of the climate reanalysis operation and by extension the accuracy of the reanalysis database had to be quantitatively measured before any further operation. For that, we rely on the following dedicated metrics (well detailed in Morley et al., 2018):

- Median Symmetric Accuracy (MSA)
- Symmetric Signed Percentage Bias (SSPB)

Figure 6 presents MSA and SSPB values for different energies between the database and RBSP-B/ECT measurements during the solar maximum year of 2014 and 2017. The solar minimum year of 2019 was not retained in the metric study due to the end of RBSP mission during that year. MSA energy profiles for both years present the same S shape evolution with a maximum MSA value around 200% obtained at low energy (below 100 keV). The profiles only differ on the minimum MSA values obtained at high energies (around 60% in 2017 and 110% in 2014). On the other hand, SSPB energy profiles come with similar bell-shaped curves with positives values almost everywhere, signalling a consistent over-estimation for both years. The unique notable difference is seen again at high energy where the 2017 SSPB becomes negative. Those results certify the precision of the database to depict evolution of the radiation belts as its accuracy for both years remain below a factor of 3. This small mismatch between the database and the assimilated data, which manifests itself by over-estimation bias can be mainly linked to the modelling of seed population injection by the external boundary condition (mentioned in Sect. 2.1). The latter is known for its strong flux intensities at high energy (Dahmen et al., 2024).

Now that the database's accuracy is assessed, we can move to the aim of the study which is proofing the use of the database as a foundation for climatology applications. For that we convert the database median and ensemble results (RD) to specification model data formats through the generation of annual energy spectra of Omnidirectional Integral Electron Fluxes (FEIO) divided by 4π (which amounts to computing isotropic averages of integral unidirectional fluxes). The selected years are 2014, 2017 and the solar minimum year of 2019. In Figure 7, the RD spectra are compared to those obtained with AE8, AE9 (1.50.001 version mean state) on four different orbits with the aim of an exhaustive description of the RD restitution in an operational situation. The orbits are : Low Earth Orbit (LEO), Highly Elliptical Orbit (HEO), Medium Earth

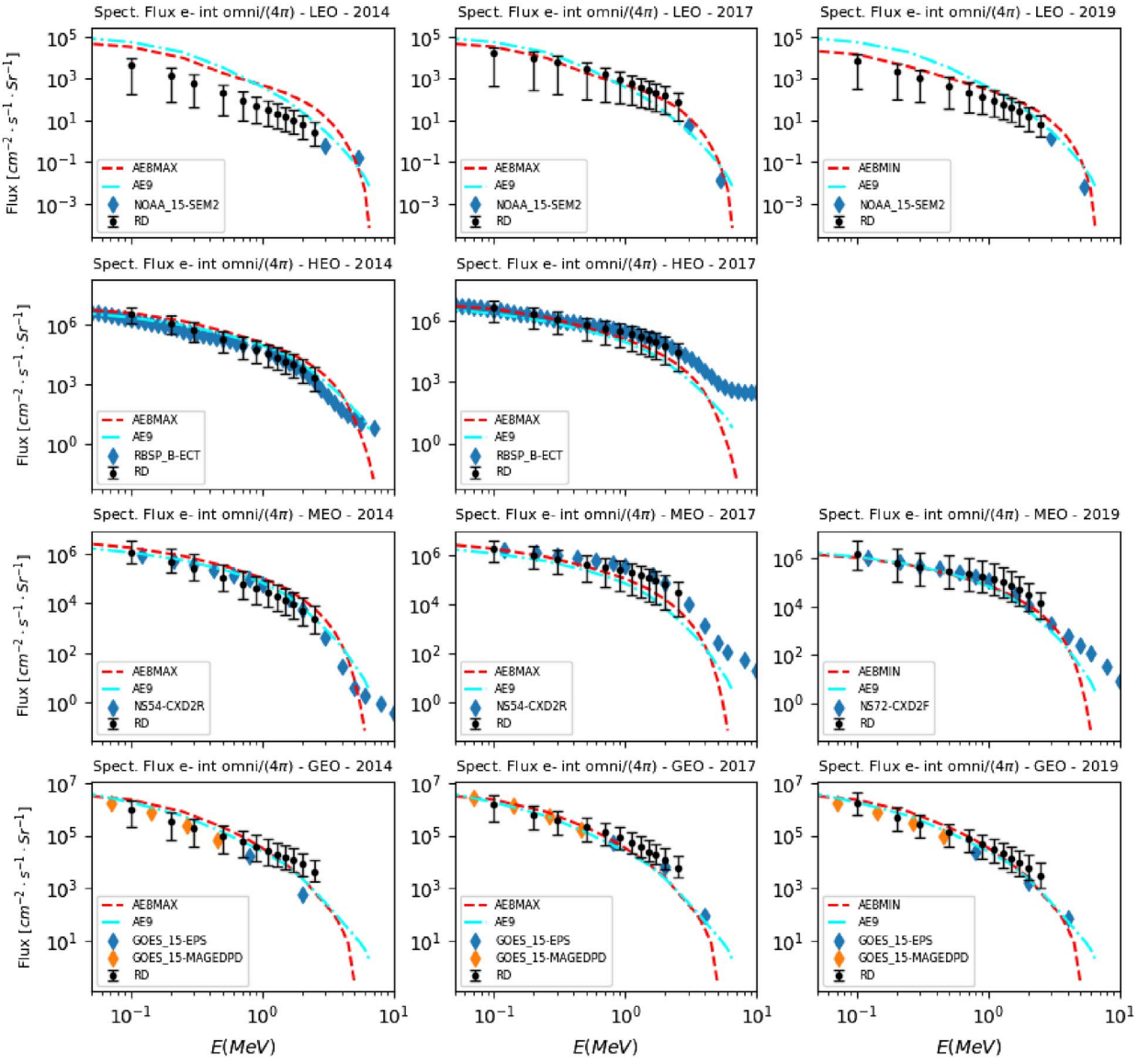

Figure 7. Energy spectrum of the FEIO fluxes divided by 4π for 2014, 2017 and 2019 (columns) at LEO, HEO, MEO and GEO orbits (rows) as seen by the AE8 model, the AE9 model, in-situ observations and the reanalysis database (RD) median and ensemble.

Table 4. Orbits and observation sources used for the generation of energy spectra to validate the reanalysis database.

Orbit	Observation sources (Satellite/instrument)	Description
LEO	NOAA-15/SEM2	Non assimilated data Electron measurements at MeV energies reconstructed from proton measurements as described in Sicard-Piet et al. (2013) and Boscher et al. (2018)
GEO	GOES15/EPS	Non assimilated data
	GOES15/MAGED	Assimilated data
MEO	GPS NS54/CXD2R	Non assimilated data
	GPS NS72/CXD2F	Assimilated data
HEO	RBSP-B/ECT	Assimilated data available only in 2014 and 2017 (mission ends in 2019)

Orbit (MEO) and the Geostationary Orbit (GEO). On each one of these orbits, the RD spectra is also compared to annual averages of observations taken from assimilated data to verify the success of the assimilation process, and when possible, non assimilated data sources, to assess the capacity of the reanalysis to reconstruct the radiation environment. All the

comparison data sources are reported in Table 4. The energy range of the simulated spectrum is limited to 100 keV–2.5 MeV, corresponding to the Salammbô-3D validity range.

Starting with the LEO orbit, the RD spectrum is below the specification models spectra in 2014 and 2019 with up to one order of magnitude of difference in 2014. In 2017, the gap narrows down and the differences with AE8 and AE9 are included within the ensemble range. Yet, the high energy branch of the 2014 and 2019 RD spectra are more consistent with the non assimilated and reconstructed electron observations from NOAA-15 which also remain below the AE8 and AE9 spectra. These results confirm the role of the low altitude model to ensure an accurate depiction of the Low Earth Orbit environment by the reanalysis database. It also shows an example of how specification models, due to their average construction, may miss yearly fluctuations.

The results on the HEO orbit mainly recall the accuracy and bias quantifications presented above in Figure 6. In fact, the spectrum inform us again on the smooth progress of the assimilation as RBSP-B/ECT observations are retrieved in the RD spectrum. As we can see, the RD median is very close to the RBSP-B/ECT data. Both of them remain within a factor of 2 of the specification models, which is coherent with the previously showed MSA values. Again, these results showcase the possible mismatch that can happen between specification models and observations especially when the solar extremum differs from typical ones, for instance a weak maximum year in 2014 (Kilpua et al., 2014).

For the MEO orbit, the RD spectrum is in accordance with the specification models with at most a mismatch of a factor 5. But for all three years, the simulation spectrum is in total accordance with the GPS N54/CXD2R observations. Knowing that GPS data (from GPS N72/CXD2F) is ingested in the simulation only from 2018, this shows that the assimilation can rely on observations from RBSP or more generally on HEO satellites to properly reconstruct this region as their orbit both sweep the same region in the heart of the outer belt around $L^* = 4$.

Finally, on the GEO orbit, the RD straight spectrum crosses the curved specification model spectra around 1 MeV and divides the energy domain in two regions. For few hundred electrons, the RD spectrum is below the specification model spectra but agrees with the assimilated observations from GOES15/MAGED. Again, this is expected as the assimilated observations should be retrieved in the restitution of RD. However, this trend reverses at high energy as the RD spectrum passes over AE8, AE9 and widen its gap even more with GOES15/EPS observations. Knowing that the GEO orbit is located around $L^* = 5.5$, this evolution is explained by the propagation of the Salammbô external boundary condition imposed at $L^* = 8$ where strong flux intensities are reported at high energy.

5 Conclusions

In this paper, we presented a long term climate reanalysis of the electron radiation belts during the last solar cycle. With this operation, we wanted to proof the use of simulated long term distributions of trapped electrons as a foundation for future climatology applications instead of sparse in-situ data. Producing specification models from climate reanalysis simulations was previously conducted on the outer belt and led to the elaboration of ONERA's OZONE specification model. Extending this operation over the whole radiation belts domain required the tackling of numerical constraints mostly in the inner zone, where spurious and non-physical artefacts might appear. For that, a low altitude empirical model was manufactured and ingested as a boundary condition in the Salammbô model. The methodology was validated against observations and alternative approaches and led to a proper reconstruction of the inner zone at the appropriate energy ranges. Using the Salammbô-EnKF code, we simulated 9 years of historical electron radiation belt dynamics starting from 2014 and generated annual energy spectra over typical orbits. Comparisons with standard models and yearly averages of in-situ observations confirmed the relevance of the climate reanalysis approach to simply extract useful average states of the radiation belts that account for yearly deviations. Yet, further statistical studies can still be conducted on the continuous distribution to provide more insights and will be the subject of a future study. Finally, although the approach is now validated and adaptable to protons (which will also be the subject of another study), any future effort to construct an operational and relevant specification model on this basis warrants a meticulous selection of the simulated period to ensure an optimal representativeness of the database. In the case of the effort presented above, it will require the extension of the simulated period located in solar cycle 24 to stronger past solar cycles.

Acknowledgements

This work received funding from the European space agency under ESA Contract 4000137689/22/NL/CRS. The authors acknowledge the NASA Van Allen Probes and Harlan E. Spence (University of New Hampshire) for use of data. RBSP-ECT data (Level 2/3, release 04) are publicly available at the website https://rbsp-ectweb.newmexicoconsortium.org/. They would like also to acknowledge the CXD team at Los Alamos National Laboratory for the GPS-NS54/CXD, GPS-NS72/CXD electron fluxes. Data access is provided by the NOAA Solar and Terrestrial Physics Branch https://www.ngdc.noaa.gov/stp/space-weather/satellite-data/satellite-systems/gps/data/). The GOES-15/MAGED and GOES-15/EPS particle data were produced in real time by the NOAA Space Weather Prediction Center (SWPC) and are distributed by the NOAA National Centers for Environmental Information (NCEI) (https://www.ncei.noaa.gov/data/goes-space-environment-monitor/access/full/2015/03/goes15/, Hanser, 2011). The NOAA-15/SEM2 particle data are publicly available at the website https://www.ncei.noaa.gov/products/poes-space-environment-monitor. Science data of the ERG (Arase) satellite were obtained from the ERG Science center operated by ISAS/JAXA and ISEE/Nagoya University https://ergsc.isee.nagoya-u.ac.jp/index.shtml.en, Miyoshi et al., 2018). PROBA1-SREM data are publicly available at the website http://srem.psi.ch/cgi-bin/srem_data_sec.cgi. The solar wind and geomagnetic indices from the OMNIWeb database are publicly available at https://omniweb.gsfc.nasa.gov/. All magnetic fields models evaluation and geomagnetic coordinates computations in this study were performed using the IRBEM (Boscher et al., 2022) and SpacePy (Morley et al., 2022) libraries. The editor thanks Gregory Cunningham and an anonymous reviewer for their assistance in evaluating this paper.

Data availability statement

The low altitude model was made publicly available on the open research repository *Zenodo* and is accessible through the following link https://zenodo.org/records/14416649 (Papadimitriou, 2024).

References

Abel, B, Thorne RM. 1998. Electron scattering loss in Earth's inner magnetosphere: 1. Dominant physical processes. *J Geophys Res Space Phys* **103 (A2)**: 2385–2396. https://doi.org/10.1029/97JA02919.

Abel, B, Thorne RM, Vampola AL. 1994. Solar cyclic behavior of trapped energetic electrons in Earth's inner radiation belt. *J Geophys Res Space Phys* **99 (A10)**: 19427–19431. https://doi.org/10.1029/94JA01626.

Anderson, BR, Millan RM, Reeves GD, Friedel RHW. 2015. Acceleration and loss of relativistic electrons during small geomagnetic storms. *Geophys Res Lett* **42 (23)**: 10113–10119. https://doi.org/10.1002/2015GL066376.

Baker, DN, Jaynes AN, Kanekal SG, Foster JC, Erickson PJ, et al. 2016. Highly relativistic radiation belt electron acceleration, transport, and loss: Large solar storm events of March and June 2015. *J Geophys Res Space Phys* **121 (7)**: 6647–6660. https://doi.org/10.1002/2016JA022502.

Beutier, T, Boscher D. 1995. A three-dimensional analysis of the electron radiation belt by the Salammbô code. *J Geophys Res Space Phys* **100 (A8)**: 14853–14861. https://doi.org/10.1029/94JA03066.

Beutier, T, Boscher D, France M. 1995. SALAMMBO: A three-dimensional simulation of the proton radiation belt. *J Geophys Res Space Phys* **100 (A9)**: 17181–17188. https://doi.org/10.1029/94JA02728.

Boscher, D, Bourdarie S, Maget V, Sicard-Piet A, Rolland G, Standarovski D. 2018. High-energy electrons in the inner zone. *IEEE Trans Nuclear Sci* **65 (8)**: 1546–1552. https://doi.org/10.1109/TNS.2018.2824543.

Boscher, D, Bourdarie S, O'Brien P, Guild T, Heynderickx D, et al. 2022. *PRBEM/IRBEM: v5.0.0*. https://doi.org/10.5281/zenodo.6867768.

Bourdarie, SA, Maget VF. 2012. *Electron radiation belt data assimilation with an ensemble Kalman filter relying on the Salammbô code*. **30**: 929–943. https://doi.org/10.5194/angeo-30-929-2012.

Bourdarie, S, Xapsos M. 2008. The near-Earth space radiation environment. *IEEE Trans Nuclear Sci* **55 (4)**: 1810–1832. https://doi.org/10.1109/TNS.2008.2001409.

Bourdarie, S, Friedel RHW, Fennell J, Kanekal S, Cayton TE. 2005. Radiation belt representation of the energetic electron environment: Model and data synthesis using the Salammbô radiation belt transport code and Los Alamos geosynchronous and GPS energetic particle data. *Space Weather* **3 (4)**. https://doi.org/10.1029/2004SW000065.

Bourdarie, S, Sicard-Piet A, Friedel R, O'Brien TP, Cayton T, Blake B, Boscher D, Lazaro D. 2009. Outer Electron Belt Specification Model. *IEEE Trans Nuclear Sci* **56 (4)**: 2251–2257. https://doi.org/10.1109/TNS.2009.2014844.

Brunet, A, Dahmen N, Katsavrias C, Santolik O, Bernoux G, et al. 2023. Improving the electron radiation belt nowcast and forecast using the safespace data assimilation modeling pipeline. *Space Weather* **21 (8)**: e2022SW003377. https://doi.org/10.1029/2022SW003377.

Caron, P, Bourdarie S, Falguere D, Lazaro D, Bourdoux P, et al. 2022. In-flight measurements of radiation environment observed by Eutelsat 7C (Electric Orbit Raising Satellite). *IEEE Trans Nuclear Sci* **69 (7)**: 1527–1532. https://doi.org/10.1109/TNS.2022.3158470.

Caron, P, Bourdarie S, Sicard A, Carron J, Calaprice M, et al. 2024. In-flight measurements of radiation environment observed by Hotbird 13F and Hotbird 13G (Electric Orbit Raising Satellites). *IEEE Trans Nuclear Sci* **71**: 1535–1541. https://doi.org/10.1109/TNS.2024.3367730.

Carpenter, DL, Anderson RR. 1992. An ISEE/whistler model of equatorial electron density in the magnetosphere. *J Geophys Res Space Phys* **97 (A2)**: 1097–1108. https://doi.org/10.1029/91JA01548.

Cervantes, S, Shprits YY, Aseev NA, Allison HJ. 2020. Quantifying the effects of EMIC Wave scattering and magnetopause shadowing in the outer electron radiation belt by means of data assimilation. *J Geophys Res Space Phys* **125 (8)**: e2020JA028208. https://doi.org/10.1029/2020JA028208.

Dahmen, N, Rogier F, Maget V. 2020. On the modelling of highly anisotropic diffusion for electron radiation belt dynamic codes. *Computer Physics Communications* **254**: 107342. https://doi.org/10.1016/j.cpc.2020.107342.

Dahmen, N, Sicard A, Brunet A, Santolik O, Pierrard V, Botek E, Darrouzet F, Katsavrias C. 2022. FARWEST: Efficient computation of wave-particle interactions for a dynamic description of the electron radiation belt diffusion. *J Geophys Res Space Phys* **127 (10)**: e2022JA030518. https://doi.org/10.1029/2022JA030518.

Dahmen, N, Brunet A, Bourdarie S, Katsavrias C, Bernoux G, et al. 2023. Electron radiation belt safety indices based on the SafeSpace modelling pipeline and dedicated to the internal charging risk. *Ann Geophys* **41 (2)**: 301–312. https://doi.org/10.5194/angeo-41-301-2023.

Dahmen, N, Sicard A, Brunet A. 2024. Climate reanalysis of electron radiation belt long-term dynamics, using a dedicated numerical scheme. *IEEE Transactions on Nuclear Science* **71**: 1598–1605. https://doi.org/10.1109/TNS.2024.3368014.

Evans, H, Bühler P, Hajdas W, Daly E, Nieminen P, Mohammadzadeh A. 2008. Results from the ESA SREM monitors and comparison with existing radiation belt models. *Adv Space Res* **42 (9)**: 1527–1537. https://doi.org/10.1016/j.asr.2008.03.022.

Evensen, G. 2003. The ensemble Kalman filter: Theoretical formulation and practical implementation. *Ocean Dyn* **53**: 343–367. https://doi.org/10.1007/s10236-003-0036-9.

Ginet, GP, O'Brien TP, Huston SL, Johnston WR, Guild TB, et al.. 2014. AE9, AP9 and SPM: New models for specifying the trapped energetic particle and space plasma environment. In: *The Van Allen Probes Mission*, N, Fox, Burch JL (Eds.), Springer, Boston, MA, USA, pp. 579–615.

Glauert, SA, Horne RB, Meredith NP. 2018. A 30-year simulation of the outer electron radiation belt. *Space Weather* **16 (10)**: 1498–1522. https://doi.org/10.1029/2018SW001981.

Goldstein, J, Angelopoulos V, De Pascuale S, Funsten HO, Kurth WS, et al. 2017. Cross-scale observations of the 2015 St. Patrick's day storm: THEMIS, Van Allen Probes, and TWINS. *J Geophys Res Space Phys* **122 (1)**: 368–392. https://doi.org/10.1002/2016JA023173.

Gubby, R, Evans J. 2002. Space environment effects and satellite design. *J Atmos Sol-Terr Phys* **64 (16)**: 1723–1733. https://doi.org/10.1016/S1364-6826(02)00122-0.

Hanser, F. 2011. *EPS/HEPAD calibration and data handbook. Tech. Rep. GOESN-ENG-048D*. https://www.ngdc.noaa.gov/stp/satellite/goes/doc/goes_nop/GOESN-ENG-048_RevD_EPS_HEPAD_13May2011.pdf.

Hedin, AE. 1987. MSIS-86 Thermospheric Model. *J Geophys Res Space Phys* **92 (A5)**: 4649–4662. https://doi.org/10.1029/JA092iA05p04649.

Herrera, D, Maget VF, Sicard-Piet A. 2016. Characterizing magnetopause shadowing effects in the outer electron radiation belt during geomagnetic storms. *J Geophys Res Space Phys* **121 (10)**: 9517–9530. https://doi.org/10.1002/2016JA022825.

Horne, R, Glauert S, Meredith N, Koskinen H, Vainio R, et al. 2013a. Forecasting the Earth's radiation belts and modelling solar energetic particle events: Recent results from SPACECAST. *J Space Weather Space Clim* **3**: A20. https://doi.org/10.1051/swsc/2013042.

Horne, RB, Glauert SA, Meredith NP, Boscher D, Maget V, Heynderickx D, Pitchford D. 2013b. Space weather impacts on satellites and forecasting the Earth's electron radiation belts with SPACECAST. *Space Weather* **11** (**4**): 169–186. https://doi.org/10.1002/swe.20023.

Horne, RB, Kersten T, Glauert SA, Meredith NP, Boscher D, Sicard-Piet A, Thorne RM, Li W. 2013c. A new diffusion matrix for whistler mode chorus waves. *J Geophys Res Space Phys* **118** (**10**): 6302–6318. https://doi.org/10.1002/jgra.50594.

Hudson, MK, Kress BT, Mueller H-R, Zastrow JA, Bernard Blake J. 2008. Relationship of the Van Allen radiation belts to solar wind drivers. *J Atmos Sol-Terr Phys* **70** (**5**): 708–729. https://doi.org/10.1016/j.jastp.2007.11.003.

Kalman, RE. 1960. A new approach to linear filtering and prediction problems. *J Basic Eng* **82** (**1**): 35–45. https://doi.org/10.1115/1.3662552.

Kilpua, E, Luhmann J, Jian L, Russell C, Li Y. 2014. Why have geomagnetic storms been so weak during the recent solar minimum and the rising phase of cycle 24? *J Atmos Sol-Terr Phys* **107**: 12–19. https://doi.org/10.1016/j.jastp.2013.11.001.

Koons, H, Mazur J, Selesnick R, Blake J, Fennell J, Roeder J, Anderson P. 1999. The impact of the space environment on space systems. *NASA STI/Recon Technical Report N,* 69, 036–69, 041. https://apps.dtic.mil/sti/pdfs/ADA376872.pdf.

Li, W, Hudson M. 2019. Earth's Van Allen radiation belts: from discovery to the Van Allen Probes era. *J Geophys Res Space Phys* **124** (**11**): 8319–8351. https://doi.org/10.1029/2018JA025940.

Li, X, Baker DN, Temerin M, Cayton TE, Reeves EGD, Christensen RA, Blake JB, Looper MD, Nakamura R, Kanekal SG. 1997. Multisatellite observations of the outer zone electron variation during the November 3–4, 1993, magnetic storm. *J Geophys Res Space Phys* **102** (**A7**): 14123–14140. https://doi.org/10.1029/97JA01101.

Li, W, Ma Q, Thorne RM, Bortnik J, Zhang X-J, et al. 2016. Radiation belt electron acceleration during the 17 March 2015 geomagnetic storm: Observations and simulations. *J Geophys Res Space Phys* **121** (**6**): 5520–5536. https://doi.org/10.1002/2016JA022400.

Li, X, Baker DN, Zhao H, Zhang K, Jaynes AN, Schiller Q, Kanekal SG, Blake JB, Temerin M. 2017. Radiation belt electron dynamics at low L (¡4): Van Allen Probes era versus previous two solar cycles. *J Geophys Res Space Phys* **122** (**5**): 5224–5234. https://doi.org/10.1002/2017JA023924.

Lorenzato, L, Sicard A, Bourdarie S. 2012. A physical model for electron radiation belts of Saturn. *J Geophys Res Space Phys* **117**: A8. https://doi.org/10.1029/2012JA017560.

Lugaz N., Liu H., Carter B. A., Gannon J., Zou S., Morley S. K.. 2023. New space companies meet a normal solar maximum. *Space Weather* **21**(**9**): E2023SW003702. https://doi.org/10.1029/2023SW003702.

Lyons, LR, Thorne RM, Kennel CF. 1972. Pitch-angle diffusion of radiation belt electrons within the plasmasphere. *J Geophys Res (1896–1977)* **77** (**19**): 3455–3474. https://doi.org/10.1029/JA077i019p03455.

Maget, V, Bourdarie S, Boscher D, Friedel RHW. 2007. Data assimilation of LANL satellite data into the Salammbô electron code over a complete solar cycle by direct insertion. *Space Weather* **5** (**10**): S10003. https://doi.org/10.1029/2007SW000322.

Maget, V, Sicard-Piet A, Bourdarie S, Lazaro D, Turner DL, Daglis IA, Sandberg I. 2015. Improved outer boundary conditions for outer radiation belt data assimilation using THEMIS-SST data and the Salammbo-EnKF code. *J Geophys Res Space Phys* **120** (**7**): 5608–5622. https://doi.org/10.1002/2015JA021001.

Meredith, NP, Horne RB, Sicard-Piet A, Boscher D, Yearby KH, Li W, Thorne RM. 2012. Global model of lower band and upper band chorus from multiple satellite observations. *J Geophys Res Space Phys* **117** (**A10**): A10225. https://doi.org/10.1029/2012JA017978.

Miyoshi, Y, Hori T, Shoji M, Teramoto M, Chang T, et al. 2018. The ERG science center. *Earth Planets Space* **70** (**1**): 1–11. https://doi.org/10.1186/s40623-018-0867-8.

Mohammadzadeh, A, Evans H, Nieminen P, Daly E, Vuilleumier P, et al. 2003. The ESA Standard Radiation Environment Monitor program first results from PROBA-I and INTEGRAL. *IEEE Trans Nuclear Sci* **50** (**6**): 2272–2277. https://doi.org/10.1109/TNS.2003.821796.

Morley, SK, Sullivan JP, Carver MR, Kippen RM, Friedel RHW, Reeves GD, Henderson MG. 2017. Energetic particle data from the global positioning system constellation. *Space Weather* **15** (**2**): 283–289. https://doi.org/10.1002/2017SW001604.

Morley, SK, Brito TV, Welling DT. 2018. Measures of model performance based on the log accuracy ratio. *Space Weather* **16** (**1**): 69–88. https://doi.org/10.1002/2017SW001669.

Morley S.K, Niehof JT, Welling DT, Larsen BA, Brunet A, et al. 2022. *SpacePy*https://doi.org/10.5281/zenodo.7083375

Nandy D. 2021. Progress in solar cycle predictions: Sunspot cycles 24–25 in perspective. *Solar Phys* **296** (**3**): 54. https://doi.org/10.1007/s11207-021-01797-2.

Nénon, Q, Sicard A, Bourdarie S. 2017. A new physical model of the electron radiation belts of Jupiter inside Europa's orbit. *J Geophys Res Space Phys* **122** (**5**): 5148–5167. https://doi.org/10.1002/2017JA023893.

Nerger, L, Hiller W, Schroter J. 2005. *PDAF – The parallel data assimilation framework: Experiences with Kalman filtering. In: Use of high performance computing in meteorology*. World Scientific, pp. 63–83. https://doi.org/10.1142/9789812701831_0006.

Nieckarz, Z, Michałek, G. 2020. Long-term observation of magnetic pulsations through the ELF Hylaty station located in the Bieszczady Mountains (south–eastern Poland). *J Space Weather Space Clim* **10**: 59. https://doi.org/10.1051/swsc/2020063,

Papadimitriou, C. 2024. *GLORAB LEO Model*. https://doi.org/10.5281/zenodo.14501659.

Pierrard, V, Lopez Rosson G, Botek E. 2019. Dynamics of megaelectron volt electrons observed in the inner belt by PROBA-V/EPT. *J Geophys Res Space Phys* **124** (**3**): 1651–1659. https://doi.org/10.1029/2018JA026289.

Ripoll, J-F, Claudepierre SG, Ukhorskiy AY, Colpitts C, Li X, Fennell JF, Crabtree C. 2020. Particle Dynamics in the Earth's radiation belts: review of current research and open questions. *J Geophys Res Space Phys* **125** (**5**): e2019JA026735. https://doi.org/10.1029/2019JA026735.

Rodger, CJ, Cresswell-Moorcock K, Clilverd MA. 2016. Nature's Grand Experiment: Linkage between magnetospheric convection and the radiation belts. *J Geophys Res Space Phys* **121** (**1**): 171–189. https://doi.org/10.1002/2015JA021537.

Roederer, JG. 1970. *Trapped particle distributions and flux mapping. In dynamics of geomagnetically trapped radiation*. Springer Berlin Heidelberg, Berlin, Heidelberg, pp. 84–111. ISBN 978-3-642-49300-3. https://doi.org/10.1007/978-3-642-49300-3_4.

Sicard, A, Bourdarie S. 2004. Physical Electron Belt Model from Jupiter's surface to the orbit of Europa. *J Geophys Res Space Phys* **109 (A2)**: A02216. https://doi.org/10.1029/2003JA010203.

Sicard, A, Boscher D, Bourdarie S, Lazaro D, Standarovski D, Ecoffet R. 2018. GREEN: the new Global Radiation Earth ENvironment model (beta version). *Ann Geophys* **36 (4)**: 953–967. https://doi.org/10.5194/angeo-36-953-2018.

Sicard-Piet, A, Bourdarie S, Boscher D, Friedel RHW, Thomsen M, Goka T, Matsumoto H, Koshiishi H. 2008. A new international geostationary electron model: IGE-2006, from 1 keV to 5.2 MeV. *Space Weather* **6 (7)**: S07003. https://doi.org/10.1029/2007SW000368.

Sicard-Piet, A, Boscher D, Lazaro D, Bourdarie S, Rolland G. 2013. *A new ONERA-CNES slot electron model*. In: 2013 14th European Conference on Radiation and Its Effects on Components and Systems (RADECS), 23–27 September 2013, Oxford, UK, pp. 1–7. https://doi.org/10.1109/RADECS.2013.6937415.

Sicard-Piet, A, Boscher D, Horne RB, Meredith NP, Maget V. 2014. Effect of plasma density on diffusion rates due to wave particle interactions with chorus and plasmaspheric hiss: extreme event analysis. *Ann Geophys* **32**: 1059–1071. https://doi.org/10.5194/angeo-32-1059-2014.

Slivinski, LC. 2018. Historical reanalysis: What, How, and Why? *J Adv Model Earth Syst* **10 (8)**: 1736–1739. https://doi.org/10.1029/2018MS001434.

Spence, HE, Reeves GD, Baker D, Blake J, Bolton M, et al. 2013. Science goals and overview of the Radiation Belt Storm Probes (RBSP) Energetic particle, Composition, and Thermal plasma (ECT) suite on NASA's Van Allen probes mission. *Space Sci Rev* **179**: 311–336. https://doi.org/10.1007/s11214-013-0007-5.

Subbotin, DA, Shprits YY, Ni B. 2011. Long-term radiation belt simulation with the VERB 3-D code: Comparison with CRRES observations. *J Geophys Res Space Phys* **116 (A12)**: A12210. https://doi.org/10.1029/2011JA017019,

Tsyganenko, N. 1989. A magnetospheric magnetic field model with a warped tail current sheet. *Planet Space Sci* **37 (1)**: 5–20. https://doi.org/10.1016/0032-0633(89)90066-4.

Tu, W, Cunningham GS, Chen Y, Morley SK, Reeves GD, Blake JB, Baker DN, Spence H. 2014. Event-specific chorus wave and electron seed population models in DREAM3D using the Van Allen Probes. *Geophys Res Lett* **41 (5)**: 1359–1366. https://doi.org/10.1002/2013GL058819.

Vette, JI. 1991. *The AE-8 trapped electron model environment*, **Vol. 91**, National Space Science Data Center (NSSDC), World Data Center A for Rockets.

Yokota, S, Ayako M, Tomoaki H. 2019. *Exploration of energization and Radiation in Geospace (ERG) MEP-i Level-3 3-D flux data*. https://doi.org/10.34515/DATA.ERG-03003.

Cite this article as: Dahmen N, Papadimitriou C, Brunet A, Sicard A, Aminalragia-Giamini S, et al. 2025. Robust reanalysis of the electron radiation belt dynamics for physics driven space climatology applications. *J. Space Weather Space Clim.* **15**, 13. https://doi.org/10.1051/swsc/2025009.